

The violent collisional history of aqueously evolved (2) Pallas

Michaël Marsset^{1,2}, Miroslav Brož³, Pierre Vernazza⁴, Alexis Drouard⁴, Julie Castillo-Rogez⁵, Josef Hanuš³, Matti Viikinkoski⁶, Nicolas Rambaux⁷, Benoît Carry⁸, Laurent Jorda⁴, Pavel Ševeček³, Mirel Birlan⁷, Franck Marchis⁹, Edyta Podlewska-Gaca^{10,11}, Erik Asphaug¹², Przemysław Bartczak¹⁰, Jérôme Berthier⁷, Fabrice Cipriani¹³, François Colas⁷, Grzegorz Dudziński¹⁰, Christophe Dumas¹⁴, Josef Ďurech³, Marin Ferrais¹⁵, Romain Fétick⁴, Thierry Fusco^{4,16}, Emmanuel Jehin¹⁵, Mikko Kaasalainen⁶, Agnieszka Kryszczyńska¹⁰, Philippe Lamy⁴, Hervé Le Coroller⁴, Anna Marciniak¹⁰, Tadeusz Michalowski¹⁰, Patrick Michel⁸, Derek C. Richardson¹⁷, Toni Santana-Ros^{18,19}, Paolo Tanga⁸, Frédéric Vachier⁷, Arthur Vigan⁴, Olivier Witasse¹³, Bin Yang²⁰

¹*Department of Earth, Atmospheric and Planetary Sciences, MIT, 77 Massachusetts Avenue, Cambridge, MA 02139, USA*

²*Astrophysics Research Centre, Queen's University Belfast, Belfast BT7 1NN, United Kingdom*

³*Institute of Astronomy, Charles University, Prague, V Holešovičkách 2, CZ-18000, Prague 8, Czech Republic*

⁴*Aix Marseille Univ, CNRS, CNES, Laboratoire d'Astrophysique de Marseille, Marseille, France*

⁵*Jet Propulsion Laboratory, California Institute of Technology, 4800 Oak Grove Drive, Pasadena, CA 91109, USA*

⁶*Mathematics and Statistics, Tampere University, 33720 Tampere, Finland*

⁷*IMCCE, Observatoire de Paris, 77 avenue Denfert-Rochereau, F-75014 Paris Cedex, France*

⁸*Université Côte d'Azur, Observatoire de la Côte d'Azur, CNRS, Laboratoire Lagrange, France*

⁹*SETI Institute, Carl Sagan Center, 189 Bernado Avenue, Mountain View CA 94043, USA*

¹⁰*Astronomical Observatory Institute, Faculty of Physics, Adam Mickiewicz University, Słoneczna 36, 60-286 Poznań, Poland*

¹¹*Institute of Physics, University of Szczecin, Wielkopolska 15, 70-453 Szczecin, Poland*

¹²*School of Earth and Space Exploration, Arizona State University, Tempe, AZ 85287, USA*

¹³*European Space Agency, ESTEC – Scientific Support Office, Keplerlaan 1, Noordwijk 2200 AG, The Netherlands*

¹⁴*TMT Observatory, 100 W. Walnut Street, Suite 300, Pasadena, CA 91124, USA*

¹⁵*Space sciences, Technologies and Astrophysics Research Institute, Université de Liège, Allée du 6 Août 17, 4000 Liège, Belgium*

¹⁶*ONERA, The French Aerospace Lab BP72, 29 avenue de la Division Leclerc, 92322 Chatillon Cedex, France*

¹⁷*Department of Astronomy, University of Maryland, College Park, MD 20742-2421, USA*

¹⁸*Departamento de Física, Ingeniería de Sistemas y Teoría de la Señal, Universidad de Alicante, E-03080 Alicante, Spain*

¹⁹*Institut de Ciències del Cosmos, Universitat de Barcelona (IEEC-UB), Martí i Franquès 1, E-08028 Barcelona, Spain*

²⁰*European Southern Observatory (ESO), Alonso de Cordova 3107, 1900 Casilla Vitacura, Santiago, Chile*

¹ **Asteroid (2) Pallas is the largest main-belt object not yet visited by a spacecraft, making its**
² **surface geology largely unknown, and limiting our understanding of its origin and collisional**

3 evolution. Previous ground-based observational campaigns returned different estimates of
4 its bulk density that are inconsistent with one another, one measurement¹ being compatible
5 within error bars with the icy Ceres ($2.16 \pm 0.01 \text{ g/cm}^3$)², and the other³ compatible within
6 error bars with the rocky Vesta ($3.46 \pm 0.03 \text{ g/cm}^3$)⁴. Here, we report high angular resolu-
7 tion observations of Pallas performed with the extreme Adaptive-Optics (AO)-fed SPHERE
8 imager⁵ on the Very Large Telescope (VLT). Pallas records a violent collisional history, with
9 numerous craters larger than 30 km in diameter populating its surface, and two large impact
10 basins that could relate to a family forming impact. Monte-Carlo simulations of the colli-
11 sional evolution of the main belt correlate this cratering record to the high average impact
12 velocity of $\sim 11.5 \text{ km/s}$ on Pallas – compared with an average of $\sim 5.8 \text{ km/s}$ for the asteroid
13 belt, induced by Pallas' high orbital inclination ($i = 34.8^\circ$) and orbital eccentricity ($e = 0.23$).
14 Compositionally, Pallas' derived bulk density of $(2.89 \pm 0.08) \text{ g/cm}^3$ is fully compatible with
15 a CM chondrite-like body as suggested by its spectral reflectance in the 3-micron wavelength
16 region⁶. A bright spot observed on its surface may indicate an enrichment in salts during an
17 early phase of aqueous alteration, compatible with Pallas relatively high albedo of 12–17%^{7,8},
18 although alternative origins are conceivable.

19 We used the sharp angular resolution ($\sim 20 \text{ mas at } 600 \text{ nm}$) of the SPHERE/ZIMPOL camera^{5,9}
20 to characterize Pallas' bulk shape and surface properties with unprecedented details and, in turn,
21 bringing new constraints on its origin and evolution. In total, 11 series of images were acquired
22 during two apparitions as part of an ESO large program¹⁰. These images provide a full surface
23 coverage, resolving ~ 120 to 130 pixels along Pallas' longest axis. The optimal angular resolu-

24 tion of each image was restored with Mistral^{11,12}, a myopic deconvolution algorithm optimized for
25 images of objects with sharp boundaries, using a parametric point-spread function¹³.

26 The deconvolved images unveil a strong surface topographic relief suggestive of a violent
27 collisional history (Fig. 1). Numerous large (~ 30 – 120 -km sized) impact features, including several
28 craters with central peaks (Supplementary Fig. 1), are ubiquitous on Pallas, forming a surface
29 reminiscent of a ‘golf ball’. A total of 36 craters larger than 30 km in diameter (D_c) identified on
30 the images (Fig. 2, Fig 3 and Supplementary Table 1), implies an *observed* average number density
31 of $N(D_c \geq 40 \text{ km}) = 4.8 \pm 0.7 \times 10^{-5} \text{ km}^{-2}$. The region with most favourable illumination in our
32 observations (Fig. 3) is more than 3 times more cratered than this average, with $N(D_c \geq 40 \text{ km}) =$
33 $1.6 \pm 0.2 \times 10^{-4} \text{ km}^{-2}$, which seems comparable to the most heavily cratered geological units on
34 Ceres¹⁴, and Vesta¹⁵ (see Methods). The similar maximum crater densities on Ceres, Pallas and
35 Vesta could indicate some degree of saturation in this diameter range. It should be noted, however,
36 that observed $D_c \geq 40 \text{ km}$ craters are relatively depleted on Ceres and Vesta, and the reported
37 crater density values in this size range are often extrapolated from the observed number of smaller
38 ($D_c \geq 1 \text{ km}$) craters by use of a model production function¹⁶. In the case of Pallas, large craters are
39 directly detected and cover a significant fraction (at least 9%) of the total surface.

40 In order to understand the heavily cratered surface of Pallas, we explored its past collisional
41 evolution, as well as that of the other two largest main-belt objects: Ceres and Vesta, through a
42 series of Monte-Carlo simulations (see Methods). In each simulation, all collisional events capa-
43 ble of producing $D_c \geq 40 \text{ km}$ craters were recorded, using the π -scaling law¹⁷ to relate the crater

44 diameter to the size of the impactor. The output of the simulations are shown in Fig. 4: The de-
45 rived synthetic crater density on Pallas, $1.9 \pm 0.5 \times 10^{-4} \text{ km}^{-2}$, turns out to be **about 2 and 3** times
46 larger than on Ceres and Vesta, respectively. Our simulations therefore hint towards the existence
47 of even more cratered units on Pallas that are not seen in the SPHERE images. The results of our
48 simulations directly reflect the different collisional environments and bulk properties of the three
49 objects, including their size, bulk density, intrinsic collisional probability and, most importantly,
50 average impact speed: while Ceres and Vesta are on rather circular and low-inclination orbits,
51 Pallas' large orbital eccentricity ($e = 0.23$) and inclination ($i = 34.8^\circ$) imply typical impact ve-
52 locities of $\sim 11.5 \text{ km/s}$ with other main-belt asteroids, versus ~ 5.1 and 5.3 km/s for the other two
53 bodies. **Such large impact velocities** of course drastically increase the number of projectiles able
54 to create large craters owing to the steep size frequency distribution of the asteroid belt (slope ap-
55 proximately -2.5 in this size range¹⁸). Specifically, the minimum impactor size needed to produce
56 a $D_c \geq 40 \text{ km}$ -size crater on Pallas is $\sim 2.4 \text{ km}$, whereas it is comprised between ~ 3.8 and $\sim 4.3 \text{ km}$
57 for the other two objects, implying a pool of 3 to 4 times more impactors for Pallas. This is only
58 partially compensated by the lower intrinsic collisional probability between Pallas and impactors
59 originating from the asteroid main belt. The heavily cratered surface of Pallas therefore appears to
60 be a natural outcome of its peculiar orbit.

61 Next, the deconvolved images were fed to the ADAM algorithm¹⁹ together with previously-
62 acquired AO images from the Keck and VLT observatories (Supplementary Table 2), and optical
63 light-curves (Supplementary Table 3), to precisely retrieve Pallas' spin orientation and 3D shape
64 (see Methods). Direct comparison between the SPHERE images and projections of the resulting

65 model are shown in Fig. 2. The model has a volume-equivalent diameter of $D = 513 \pm 6$ km.
66 Semi-axes along the principal axes of inertia $(284 \times 266 \times 224) \pm 6$ km indicate significant departure
67 from hydrostatic equilibrium considering Pallas' current rotation period of 7.8 h (see Methods and
68 Supplementary Fig. 2). This deviation can be explained by a substantial flattening of the South
69 Pole of Pallas (Supplementary Fig. 3) that could relate to the existence of an ancient impact basin,
70 similar to Rheasilvia on Vesta, and by a change of its rotation period, from ~ 6.2 h to 7.8 h, during
71 such a basin-forming impact. The South-pole basin would represent $6 \pm 1\%$ of the current volume
72 of Pallas, which is significantly larger than the volume of Rheasilvia ($\sim 3 \pm 1\%$ of the total volume
73 of Vesta²⁰). Another large excavation, roughly 1% the volume of Pallas, is found near its equator
74 (Fig. 2). Using a Smoothed-Particle Hydrodynamics (SPH) code to model the formation of the
75 basins and their ejected fragments, we found that the size and volume of the equatorial basin are
76 best reproduced assuming a large oblique impact with a 60–90-km-sized projectile (see Methods).
77 Simulations of the subsequent orbital and collisional evolution of the resulting fragment population
78 aligns well both with the orbital distribution and size frequency distribution (SFD) of the current
79 Pallas family after $1.7^{+0.2}_{-0.4}$ Ga evolution. This implies the equatorial basin could very well be the
80 remnant of the Pallas family forming event. Similar simulations for the South-pole basin, on the
81 other hand, suggest it does not relate to the present-day family.

82 Combining the volume measured from our 3-D shape model with available mass estimates
83 (average value $(2.04 \pm 0.03) \times 10^{20}$ kg; see Methods, Supplementary Fig. 4 and Supplemen-
84 tary Table 4) yields a density of 2.89 ± 0.08 g/cm³, significantly different from that of both Ceres
85 $(2.16 \pm 0.01$ g/cm³)² and Vesta $(3.46 \pm 0.03$ g/cm³)⁴, suggesting a distinct bulk composition for Pal-

86 las. In particular, Pallas' higher density with respect to Ceres is most likely explained by a lower
87 internal water-to-rock fraction, which is also consistent with Pallas' higher and seemingly more
88 stable topography. Further, assuming an interior with little porosity, Pallas' density is fully com-
89 patible with the average grain density of CM chondrite meteorites ($2.90 \pm 0.08 \text{ g/cm}^3$)²¹, Pallas'
90 closest spectral analogues in the 3-micron spectral region⁶. This opens the possibility that Pal-
91 las accreted from the same starting material as the CM-like Ch and Cgh-type asteroids²². In this
92 scenario, spectral differences between these bodies over the visible and near-infrared wavelengths
93 would result from distinct subsequent thermal and impact evolutions, owing to the larger size of
94 Pallas and its unique collisional environment (see additional discussion in Methods).

95 A similar formation time for Pallas and the CM chondrites (3-4 Ma after the formation of
96 Calcium-Aluminium-rich Inclusions, CAIs)²³ would imply that the interior of Pallas never reached
97 the silicate dehydration temperature ($\sim 820 \text{ K}$) necessary to trigger the differentiation of a denser
98 silicate core below a hydrated mantle, implying it has a rather homogeneous interior (see Meth-
99 ods and Supplementary Fig. 5). However, given Pallas' large size, partial differentiation (i.e.,
100 separation of water from silicates and upward flow) must have occurred in its interior, leading to
101 an enrichment in salts that could explain Pallas' high albedo ($p_v = 12\text{--}17\%$)^{7,8} with respect to
102 Ch/Cgh-type asteroids ($p_v = 6 \pm 2\%$)²⁴. The presence of a bright spot with $\sim 10\%$ brightness en-
103 hancement on Pallas (Fig. 1) reminiscent of those found on Ceres²⁵, may provide additional support
104 to the existence of salt deposits on its surface. However, alternative origins, such as the accretion
105 of a bright exogenic material (e.g., ordinary chondrite) or the presence of unresolved ejecta blan-
106 ket of a fresh impact that excavated bright material from the subsurface, cannot presently be ruled

107 out. Considering that some studies proposed that the near-Earth object Phaethon originated
108 from Pallas^{26,27} (see discussion in Methods), we hypothesise that the presence of salts (there-
109 fore sodium) in Pallas is at the origin of the unusual diversity of sodium content measured in the
110 Geminid meteors stream^{28–32} emitted by Phaethon³³.

- 112 1. Schmidt, B. E. *et al.* The Shape and Surface Variation of 2 Pallas from the Hubble Space
113 Telescope. *Science* **326**, 275–278 (2009).
- 114 2. Park, R. S. *et al.* A partially differentiated interior for (1) Ceres deduced from its gravity field
115 and shape. *Nature* **537**, 515–517 (2016).
- 116 3. Carry, B. *et al.* Physical properties of (2) Pallas. *Icarus* **205**, 460–472 (2010).
- 117 4. Russell, C. T. *et al.* Dawn at Vesta: Testing the Protoplanetary Paradigm. *Science* **336**, 684–
118 686 (2012).
- 119 5. Beuzit, J. L. *et al.* SPHERE: the exoplanet imager for the Very Large Telescope. *Astron.*
120 *Astrophys.* **631**, A155 (2019). 1902.04080.
- 121 6. Larson, H. P., Feierberg, M. A. & Lebofsky, L. A. The composition of asteroid 2 Pallas and
122 its relation to primitive meteorites. *Icarus* **56**, 398–408 (1983).
- 123 7. Tedesco, E. F., Noah, P. V., Noah, M. & Price, S. D. The Supplemental IRAS Minor Planet
124 Survey. *Astron. J.* **123**, 1056–1085 (2002).
- 125 8. Alí-Lagoa, V., Müller, T. G., Usui, F. & Hasegawa, S. The AKARI IRC asteroid flux catalogue:
126 updated diameters and albedos. *Astron. Astrophys.* **612**, A85 (2018). 1712.07496.

- 127 9. Thalmann, C. *et al.* SPHERE ZIMPOL: overview and performance simulation. In *Ground-*
128 *based and Airborne Instrum. for Astron. II*, vol. 7014 of *Proc. SPIE*, 70143F (2008).
- 129 10. Vernazza, P. *et al.* The impact crater at the origin of the Julia family detected with
130 VLT/SPHERE? *Astron. Astrophys.* **618**, A154 (2018).
- 131 11. Fusco, T. *et al.* *Deconvolution of astronomical images obtained from ground-based telescopes*
132 *with adaptive optics*, vol. 4839 of *Soc. of Photo-Optical Instrum. Eng. (SPIE) Conf. Series*,
133 1065–1075 (2003).
- 134 12. Mugnier, L. M., Fusco, T. & Conan, J.-M. MISTRAL: a myopic edge-preserving image
135 restoration method, with application to astronomical adaptive-optics-corrected long-exposure
136 images. *J. Opt. Soc. Am. A* **21**, 1841–1854 (2004).
- 137 13. Fétick, R. J. *et al.* Closing the gap between Earth-based and interplanet. mission observations:
138 Vesta seen by VLT/SPHERE. *Astron. Astrophys.* **623**, A6 (2019). 1902.01287.
- 139 14. Scully, J. E. C. *et al.* Ceres' Ezinu quadrangle: a heavily cratered region with evidence for
140 localized subsurface water ice and the context of Occator crater. *Icarus* **316**, 46–62 (2018).
- 141 15. Schmedemann, N. *et al.* The cratering record, chronology and surface ages of (4) Vesta in
142 comparison to smaller asteroids and the ages of HED meteorites. *Planet. Space Sci.* **103**,
143 104–130 (2014).
- 144 16. Hiesinger, H. *et al.* Cratering on Ceres: Implications for its crust and evolution. *Science* **353**,
145 aaf4759-1-aaf4759-8 (2016).

- 146 17. Melosh, H. J. *Impact cratering: A geologic process* (New York, Oxford University Press,
147 1989).
- 148 18. Gladman, B. J. *et al.* On the asteroid belt's orbital and size distribution. *Icarus* **202**, 104–118
149 (2009).
- 150 19. Viikinkoski, M., Kaasalainen, M. & Durech, J. ADAM: a general method for using various
151 data types in asteroid reconstruction. *Astron. Astrophys.* **576**, A8 (2015).
- 152 20. Schenk, P. *et al.* The Geologically Recent Giant Impact Basins at Vesta's South Pole. *Science*
153 **336**, 694–697 (2012).
- 154 21. Consolmagno, G., Britt, D. & Macke, R. The significance of meteorite density and porosity.
155 *Chem Erde-Geochem* **68**, 1–29 (2008).
- 156 22. Vernazza, P. *et al.* Compositional Homogeneity of CM Parent Bodies. *Astron. J.* **152**, 54
157 (2016).
- 158 23. Doyle, P. M. *et al.* Early aqueous activity on the ordinary and carbonaceous chondrite parent
159 bodies recorded by fayalite. *Nat. Commun.* **6**, 7444 (2015).
- 160 24. Masiero, J. R. *et al.* Preliminary Analysis of WISE/NEOWISE 3-Band Cryogenic and Post-
161 cryogenic Observations of Main Belt Asteroids. *Astrophys. J.* **759**, L8 (2012). 1209.5794.
- 162 25. Nathues, A. *et al.* Sublimation in bright spots on (1) Ceres. *Nature* **528**, 237–240 (2015).
- 163 26. de León, J., Campins, H., Tsiganis, K., Morbidelli, A. & Licandro, J. Origin of the near-Earth
164 asteroid Phaethon and the Geminids meteor shower. *Astron. Astrophys.* **513**, A26 (2010).

- 165 27. Todorović, N. The dynamical connection between Phaethon and Pallas. *Mon. Not. R. Astron.*
166 *Soc.* **475**, 601–604 (2018). 1801.08857.
- 167 28. Trigo-Rodríguez, J. M., Llorca, J., Borovička, J. & Fabregat, J. Spectroscopy of a Geminid
168 Fireball: its Similarity to Cometary Meteoroids and the Nature of its Parent Body. *Earth Moon*
169 *Planets* **95**, 375–387 (2004).
- 170 29. Borovička, J., Koten, P., Spurný, P., Boček, J. & Štork, R. A survey of meteor spectra and
171 orbits: evidence for three populations of Na-free meteoroids. *Icarus* **174**, 15–30 (2005).
- 172 30. Borovička, J. Spectroscopic Analysis of Geminid Meteors. In Rendtel, J. & Vaubaillon, J.
173 (eds.) *Proc. of the Int. Meteor Conf., 26th IMC, Barges, France, 2007*, 42–51 (2010).
- 174 31. Kasuga, T., Watanabe, J. & Ebizuka, N. A 2004 Geminid meteor spectrum in the visible-
175 ultraviolet region. Extreme Na depletion? *Astron. Astrophys.* **438**, L17–L20 (2005).
- 176 32. Kasuga, T. Thermal Evolution of the Phaethon-Geminid Stream Complex. *Earth Moon Plan-*
177 *ets* **105**, 321–326 (2009).
- 178 33. Whipple, F. L. 1983 TB and the Geminid Meteors. *IAU Circulars* **3881** (1983).

179 **Acknowledgements** Based on observations collected at the European Organisation for Astronomical Re-
180 search in the Southern Hemisphere under ESO programme 199.C-0074 (PI: P.V.). This research has made
181 use of the Keck Observatory Archive (KOA), which is operated by the W. M. Keck Observatory and the
182 NASA Exoplanet Science Institute (NExSci), under contract with the National Aeronautics and Space Ad-
183 ministration. M.M. was supported by the National Aeronautics and Space Administration under Grant

184 No. 80NSSC18K0849 issued through the Planetary Astronomy Program. This work was supported by the
185 French Direction Générale de l'Armement (DGA) and Aix-Marseille Université (AMU). P.V., A.D. and
186 B.C. were supported by CNRS/INSU/PNP. J.H., J.Ď. and P.Š. were supported by the grant 18-09470S of
187 the Czech Science Foundation and by the Charles University Research Programme No. UNCE/SCI/023.
188 M.Brož was supported by the grant 18-04514J of the Czech Science Foundation. This project has received
189 funding from the European Union's Horizon 2020 research and innovation programme under grant agree-
190 ment No. 730890. This material reflects only the authors' views and the Commission is not liable for any
191 use that may be made of the information contained herein.

192 **Author contributions** P.V. is the Principal Investigator of the ESO large survey that acquired the images
193 of Pallas. M.M. and P.V. designed and operated the survey in service mode. M.M. led the research on
194 Pallas. M.M., P.V., R.F. and T.F. reduced and deconvolved the SPHERE images. A.D. performed the crater
195 analysis. M.Brož analysed the Pallas family and ran the N-body and SPH simulations. D.C.R and E.A.
196 provided some of the numerical codes used for the simulations. B.C. and J.H. retrieved earlier disk-resolved
197 and disk-integrated data for Pallas from the literature. M.V. and J.H. reconstructed the 3D shape of Pallas.
198 N.R. and L.J. analysed the shape. B.C. provided the mass estimate. J.C. performed the compositional
199 analysis and thermophysical modelling of Pallas. M.M., M.Brož, P.V. and J.C. worked jointly to write the
200 manuscript. All authors discussed the results and commented on the manuscript.

201 **Competing Interests** The authors declare that they have no competing financial interests.

202 **Correspondence** Correspondence and requests for materials should be addressed to M. Marsset (email:
203 mmarsset@mit.edu).

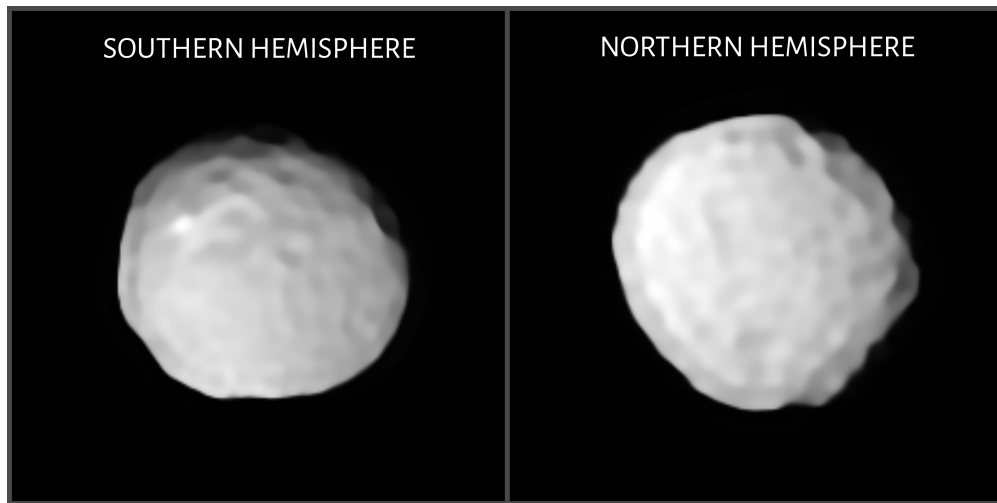


Figure 1: **The two hemispheres of (2) Pallas as seen by VLT/SPHERE.** Images taken on UT October 28 2017 (southern hemisphere) and UT March 15 2019 (northern hemisphere). Numerous large craters are visible on both hemispheres, and a bright spot reminiscent of salt deposits on Ceres is found on the southern one.

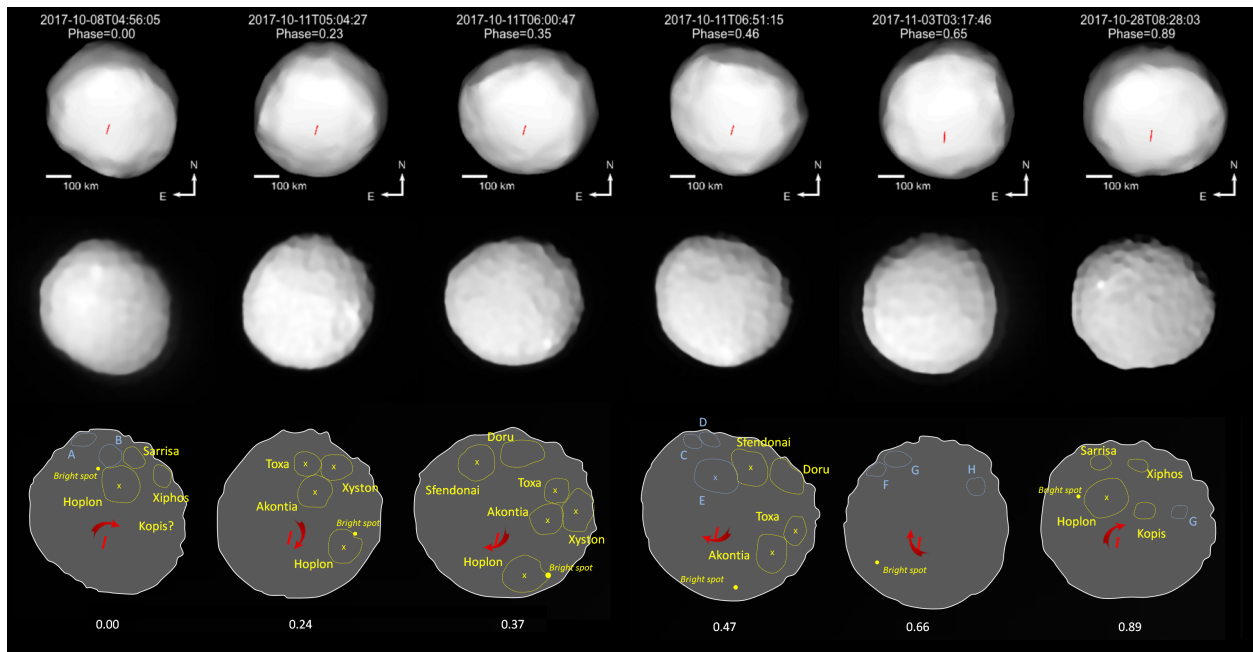


Figure 2: **Deconvolved images of (2) Pallas (middle line), compared to projections of the ADAM shape model (top) and sketches highlighting the main geological features identified on Pallas (bottom).** The first panel corresponds to the southern hemisphere and the bottom one to its northern hemisphere. Features detected at a single epoch are shown in blue, and those tracked throughout multiple rotation phase angles are in yellow. The epochs are ordered by increasing rotation phase. The red segment indicates Pallas' spin axis.

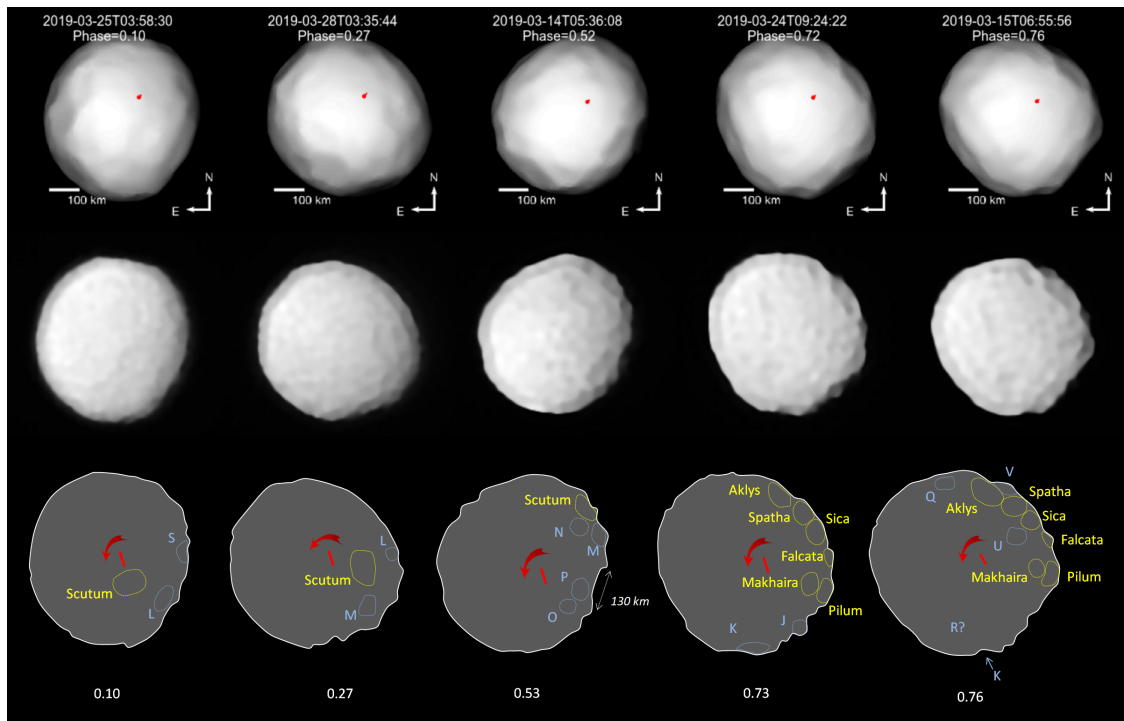


Figure 2: *continued.*

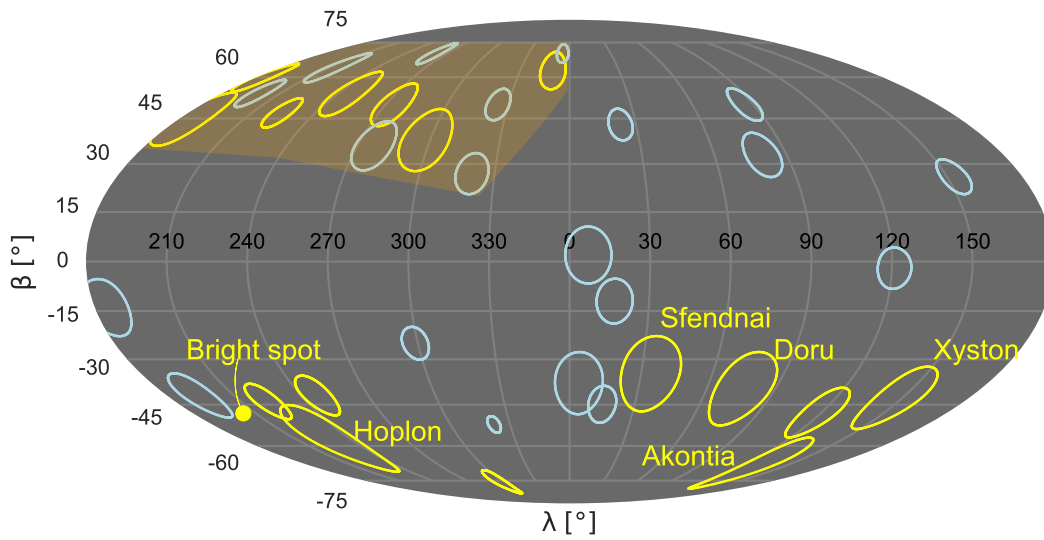


Figure 3: **Mollweide projection of the 36 craters and the bright spot identified on the surface of Pallas.** The same colour code as in Fig. 2 is used for the craters. The highly cratered region is highlighted in light orange. The name of the five largest craters is indicated.

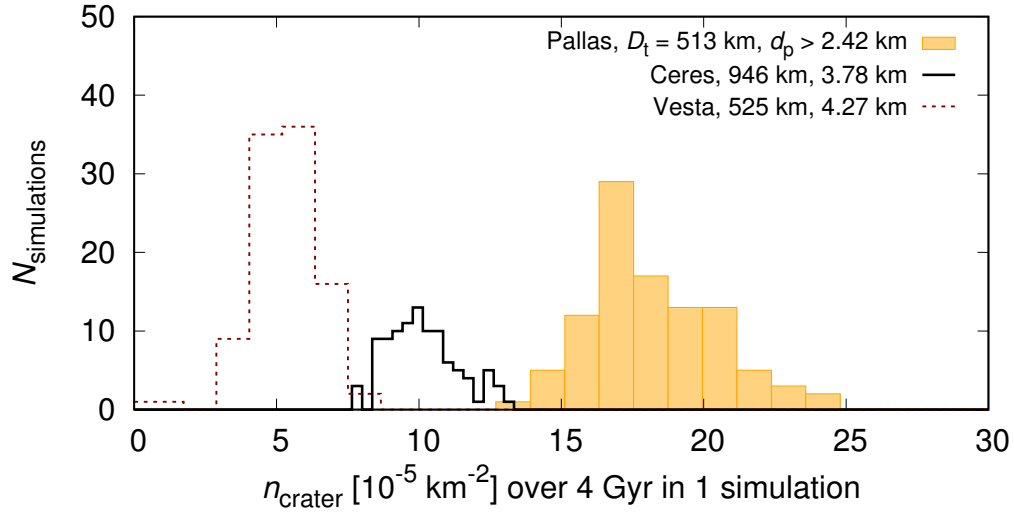


Figure 4: **N-body simulations link the heavily cratered surface of Pallas to its highly inclined and eccentric orbit inducing high average impact speed on this body.** The histograms show the number of collisional events per surface unit able to create a crater with $D_c \geq 40$ km for each of the three largest asteroids: (1) Ceres, (4) Vesta, and (2) Pallas. A total of 100 Monte-Carlo simulations were ran for each object. The target size D_t and the projectile diameter d_p needed to create the craters are provided in the legend. The high impact rate per surface unit on Pallas reflects its large median impact velocity of $v_{\text{imp}} = 11.5 \text{ km s}^{-1}$, compared to the typical velocity of $\sim 5.8 \text{ km s}^{-1}$ for the main belt.

204 **Methods**

205 **Cratering on Pallas.** Pallas exhibits numerous large ($D_c > 30$ km) impact features, including
206 various complex craters showing evidence for a central peak (Supplementary Fig. 1). The nearly
207 pole-on orientation of the asteroid during our 11 sets of SPHERE observations – 6 for the south-
208 ern hemisphere and 5 for the northern one – allowed to accurately identify the craters on both
209 hemispheres throughout a complete rotational phase period.

210 We first removed the brightness gradient from each SPHERE image, which depends on the
211 local illumination (local incidence, reflection and phase angle), following the method outlined
212 in Fétick et al (2019)¹³. The craters were then visually searched on the images, simultaneously
213 using a projection of the ADAM shape model to measure their planetocentric coordinates. Owing to
214 imperfect AO corrections and deconvolution of the images, many features that could be interpreted
215 as craters might actually be artefacts and/or correlated noise in the images. To avoid false positives,
216 each series of observation was carefully examined, and only features consistently present across a
217 full set of images were recorded. Specifically, each sequence of SPHERE observations consisted in
218 5 images being simultaneously recorded by the two ZIMPOL cameras⁹, resulting in a total set of 10
219 images per observing epoch. Confirmed craters are those found throughout at least one complete
220 sequence of 10 images.

221 We then measured the crater diameter by extracting their brightness profile on the image. We
222 defined the crater edge as the location where the profile inflects symmetrically on both sides of the
223 centre of the crater. Diameters were estimated as the distance between the two opposite ends of

224 the edge, orthogonally to the direction of the sub-solar point to account for the viewing angle. For
225 those craters that are visible at multiple epochs of observation, we checked the consistency of our
226 method by comparing values computed from the different epochs.

227 Using this method, a total of 36 craters were identified on Pallas, including 34 with diameter
228 $D_c \geq 40$ km (Supplementary Table 1). Considering our careful rejection of possible false positives,
229 which probably led to the rejection of a few true features, this number should be considered as
230 a lower limit. In addition, several craters located near the sub-solar point, where shadowing was
231 minimal, might have been also missed. Anyhow, using our volume-equivalent diameter of $D =$
232 513 km, the number of 34 craters translates to an *observed* average number density of $N(D_c \geq$
233 40 km) = $4.1 - 5.5 \times 10^{-5} \text{ km}^{-2}$, i.e., more than twice larger than the average crater density on Vesta
234 in this size range³⁵. The interval of values provided here reflects the uncertainty on the surface of
235 Pallas properly sampled by SPHERE: while the full surface was covered, the equatorial region
236 was seen almost edge-on owing to the nearly pole-on orientation of Pallas during our observations.
237 This likely explains the apparent lack of craters located between planetocentric latitudes of -15
238 and +15° (Fig. 3). This region representing ~25% of the total surface of Pallas, we assumed that
239 between 75–100% of the surface was accurately covered by our observations, and propagated this
240 assumption to the uncertainty on crater density. Global crater frequency measurements however
241 do not make a lot of sense, because they average crater counts over multiple geological units with
242 different ages. The most heavily cratered area of Pallas is found in the north-west region, between
243 approximately $\lambda=180-0^\circ$, $\beta=35-75^\circ$ (Fig. 3). This region represents an area of 7.2 to $9.3 \times 10^4 \text{ km}^2$
244 and contains 13 craters larger than 40 km in diameter (14 larger than 30 km), implying a crater

245 number density $N(D_c \geq 40 \text{ km}) = 1.6 \pm 0.2 \times 10^{-4} \text{ km}^{-2}$. This is comparable to the oldest
246 and most heavily cratered terrains (HCT) found on Ceres and Vesta, such as the cratered terrain
247 of Ceres’s Ezinu quadrangle, with $N(D_c \geq 45 \text{ km}) = 1.4 \times 10^{-4} \text{ km}^{-2}$,¹⁴ and the North pole of
248 Vesta, with $N(D_c \geq 40 \text{ km}) = 1.5 \times 10^{-4} \text{ km}^{-2}$.¹⁵ The vast majority of geological units on Ceres
249 and Vesta are far less cratered^{14–16,36–38}.

250 **Modelled cratering record.** To understand the origin of the heavily cratered surface of Pal-
251 las, we explored its 4-Ga-long collisional evolution, as well as that of (1) Ceres and (4) Vesta,
252 through series of Monte–Carlo simulations performed with the Boulder code^{39,40}. The expected
253 crater density on the three objects was evaluated by extracting all relevant collisional events in
254 an extended set of 100 simulations per object. Specifically, using the π -scaling¹⁷ for the relation
255 $D_c(d_p)$ between the crater and projectile sizes, we recorded all events able to produce $D_c \geq 40 \text{ km}$
256 in order to allow a direct comparison between simulations and observations. The projectile size
257 needed to create a given crater size and, therefore, the frequency of large collisions in our simula-
258 tions highly depends on the choice of the scaling law⁴¹. However, the resulting *relative* differences
259 between the three bodies (Ceres, Vesta and Pallas) is likely minor when using the same scaling law
260 for all of them.

261 Collisional probabilities (P_i) and impact velocities (v_{imp}) were computed from the observed
262 orbital distribution of the main belt, and an evolving size-frequency distribution (SFD) provid-
263 ing the best match to the observed SFD after 4 Ga evolution. Relevant input parameters of our
264 simulations were computed from the current osculating orbital elements of the asteroids and are

265 summarised in Supplementary Table 5. Using proper orbital elements instead of the osculating
 266 ones does not change significantly the value of the derived parameters. For instance, in the
 267 case of Pallas, we derived $P_i = 2.17 \times 10^{-18} \text{ km}^{-2} \text{ a}^{-1}$ and $v_{\text{imp}} = 11.49 \text{ km/s}$ when using current
 268 elements ($e = 0.23$, $i = 34.8^\circ$), and $P_i = 1.89 \times 10^{-18} \text{ km}^{-2} \text{ a}^{-1}$ and $v_{\text{imp}} = 11.25 \text{ km/s}$ for proper el-
 269 ements ($e = 0.28$, $i = 33.2^\circ$), implying a variation of $\sim 10\%$ and $\sim 2\%$, respectively. The result-
 270 ing synthetic crater densities for Ceres, Vesta and Pallas are as followed: $10 \pm 3 \times 10^{-5} \text{ km}^{-2}$,
 271 $6 \pm 3 \times 10^{-5} \text{ km}^{-2}$, and $19 \pm 5 \times 10^{-5} \text{ km}^{-2}$, respectively (Fig. 4). Here, the range of values reflect
 272 the Poisson uncertainty due to the stochasticity of the collisional process.

273 The derived estimates directly relate to the different collisional environment of the three
 274 objects. In particular, Pallas is located in a more violent environment due to its eccentric ($e = 0.23$)
 275 and highly-inclined ($i = 34.8^\circ$) orbit that implies substantially larger impact velocities v_{imp} . This,
 276 of course, increases the number of available projectiles, because d_p needed to create $D_c \geq 40 \text{ km}$
 277 is smaller, and the size frequency distribution (SFD) of the asteroid belt is steep (slope -2.5 in this
 278 size range¹⁸). This is only partially compensated by the lower intrinsic probability of collisions
 279 between Pallas and impactors from the asteroid belt. Ceres is about twice larger than the other
 280 two bodies but gravitational focussing, expressed as $f_g = 1 + (v_{\text{esc}}/v_{\text{imp}})^2 \doteq 1.01$, where v_{esc} is the
 281 escape velocity and v_{imp} the impact velocity, does not contribute significantly.

282 **3D shape reconstruction.** We used the All-Data Asteroid Modeling (ADAM) inversion procedure^{19,42–45}
 283 to reconstruct the shape and spin of Pallas, using as input the complete set of disk-resolved im-
 284 ages and optical lightcurves listed in Supplementary Tables 2 and 3, respectively, and occultation

285 data described in Hanuš et al. (2017)⁴⁵ for sanity checks. Our set of images comprises both our
286 VLT/SPHERE observations, as well as Keck/NIRC2 images retrieved from the Keck Observatory
287 Archive (KOA). While the NIRC2 images have a lower angular resolution than the SPHERE ones,
288 these images sample additional observing geometries of Pallas that are complementary to our own
289 dataset for shape reconstruction. We first created a low-resolution shape model using the spherical
290 harmonics parameterization and our complete dataset of images and light curves as input. Due
291 to the disparity in imaging resolution of the Keck/NIRC2⁴⁶ and VLT/SPHERE^{5,9} images, we then
292 constructed a higher resolution model from the SPHERE data only, using the low-resolution shape
293 model as initial input. Finally, we allowed the vertices to move independently of parameterization,
294 subject only to the regularization and AO data fit functions.

295 Overall, our model fits the image boundaries at the sub-pixel level and recovers most of the
296 high-resolution features present in the SPHERE images (Fig. 2). The best triaxial ellipsoid fit to
297 the 3D-shape model has a volume-equivalent diameter of $D=513\pm 6$ km, with semi-axes along the
298 principal axes of inertia $(284\times 266\times 224)\pm 6$ km. An equator-on projection of the model reveals that
299 the South Pole is substantially flattened (Supplementary Fig. 3), which could relate to the existence of
300 a large basin, possibly created by a single or a few significant impacts, like Rheasilvia on Vesta²⁰.
301 This feature is unseen on the SPHERE images, due to the nearly pole-on orientation of the asteroid
302 during the observations, and could only be retrieved thanks to the 3D-shape reconstruction and the
303 use of complementary light curves. The basin would represent $\sim 6 \pm 1\%$ of the current volume
304 of Pallas. Its polar location is consistent with reorientation of the rotation axis towards maximum
305 moment of inertia, which occurs over timescales of the order of $\sim 10^5$ a for a Pallas-size body⁴⁷.

306 **The fossile shape of Pallas.** Our ADAM shape model was further used to investigate the
307 hydrostatic shape of (2) Pallas, assuming both an homogeneous and a two-layer differentiated
308 interior. The hydrostatic equilibrium figure of a homogeneous body can be computed using the
309 MacLaurin equation, whereas for a differentiated body it requires to be solved numerically. Here,
310 we used a numerical integration of the Clairaut's equations developed to an order that depends
311 on the geodetic parameter $m^{48,49}$ that is function of the angular spin velocity and mean density of
312 the body. Depending on the value of that parameter and the accuracy of available observations,
313 the Clairaut's equations may be developed to first, second or third order⁵⁰. This method has been
314 previously applied to the hydrostatic figures of the Earth⁴⁸ and Ceres^{2,49}.

315 Supplementary Fig. 2 compares the (a-c) dimension of Pallas with respect to a similar-size
316 body at equilibrium, where a and c are the equatorial and polar radii of the object. The shape
317 of Pallas significantly deviates from equilibrium considering its current rotation period (~7.8 h),
318 implying it was significantly reshaped by a large impact, and/or that it used to rotate faster in the
319 past. We investigated whether the putative South Pole basin could account for this deviation. To
320 do so, a best-fit ellipsoid was adjusted to the 3D-shape model of Pallas, excluding the South Pole
321 (specifically, meshes below -31° latitudes were rejected from the fit; Supplementary Fig. 3). The
322 resulting ellipsoid has semi-major axis $282 \times 262 \times 249$ km, which is closer to an hydrostatic shape,
323 but still requires a change of rotation period of 1.6 h, down to ~6.2 h, to be at equilibrium.

324 For a homogeneous sphere, the change in angular momentum is given by $\Delta L = 2/5 M R^2 2\pi/|P-$
325 $P'|$, where M is the mass, R the radius and P the rotation period. If we simply assume $\Delta L =$

326 $m_p v_{\text{imp}} \sin(45^\circ) R$, where subscript p refers to ‘projectile’, and express $d_p = 2 \times [3m_p/(4\pi\rho_p)]^{1/3}$,
327 then the projectile size needed for $|P - P'| = 1.6$ h is $d_p \approx 48$ km assuming $\rho_p = 3\,000$ kg m⁻³ and
328 $v_{\text{imp}} = 11.5$ km/s. This translates to a crater size of ~ 370 km according to the π -scaling law¹⁷, i.e.,
329 $\sim 70\%$ of the current size of Pallas, which could represent the South-pole basin. Therefore, it seems
330 very plausible that the fitted ellipsoid in Supplementary Fig. 3 represents the original, pre-impact
331 shape of Pallas.

332 **The present-day Pallas family.** Pallas is surrounded by a few hundreds small ($D < 20$ km-
333 sized) bodies that together form a distinct asteroid family⁵¹. We describe here the method we used
334 to identify the family members, whose orbital properties were subsequently used to examine the
335 physical conditions of the family forming event.

336 The Pallas family is well-defined and taxonomically homogeneous. It is located at high in-
337 clination, where few background asteroids exist. The geometric albedo of the family members is
338 comprised in the range $p_V \in (0.06; 0.24)$ ⁵², and colours from the SDSS⁵³ are such that the colour
339 index $a^* < 0$ mag. The dynamic environment of Pallas is complex and affected by several mean-
340 motion and secular resonances. As a consequence, many asteroids are on chaotic, unstable or
341 resonant orbits, with proper orbital elements that can quickly shift in eccentricity and/or inclina-
342 tion. Because of this, many family members can be missed when identifying them using proper
343 elements. We therefore instead chose to consider the averaged mean orbital elements of the aster-
344 oids, including all forced terms. The mean elements were computed carefully to avoid aliasing of
345 fast orbital frequencies, with a four-stage convolution filter based on the Kaiser windows⁵⁴. Input

346 sampling of the osculating elements was set to 1 year, and we used four filters denoted A, A, A,
347 B with decimation factors 10, 10, 5, 3, resulting in output sampling of the mean elements of 1500
348 years. Finally, we applied a running-average filter with window 1 Ma and output sampling 0.1 Ma.
349 Using this method, we were able to use all of the observed multi-opposition asteroids, not only
350 those with stable proper elements (473 vs 319 bodies). We used *exactly* the same algorithm for our
351 synthetic families generated for investigating the orbital evolution of the Pallas family through N-
352 body simulations (see below), allowing a direct comparison of our simulations with observations.
353 Supplementary Fig. 6 displays the mean orbital elements of the observed population of the family
354 members, interlopers and background asteroids in the vicinity of Pallas.

355 **Orbital evolution of the family.** The long-term orbital evolution of the Pallas family was
356 studied by use of the symplectic N-body integrator Swift-Rmvs3⁵⁵ in order to estimate the age of
357 the family. We explored the simplest case in which the current family was created in a single large
358 collision. More complicated scenarios, e.g., in which the family was subsequently rejuvenated by
359 smaller impacts, are beyond the scope of this work. Our dynamical model⁵⁶ included the outer solar
360 system planets, and a barycentric correction to account for the inner planets. Pallas was treated as
361 a massive body, as close encounters can enhance diffusion in its vicinity. Our code further included
362 the Yarkovsky diurnal and seasonal effects^{57,58}, the YORP effect⁵⁹, and reorientation or reshaping
363 during random collisions and when bodies reach a critical spin rate. The time step was set to
364 $\Delta t = 36.525$ d, and the time spanned up to 4 Ga.

365 We created a synthetic family of 1380 bodies with assumed isotropic velocities⁶⁰ and spins,

366 escape velocity $v_{\text{esc}} = 324 \text{ m s}^{-1}$, and maximum velocity difference $v_{\text{max}} = 600 \text{ m s}^{-1}$. We derived
367 the preferred true anomaly $f = 140^\circ$ and argument of perihelion $\omega = 60$ at the time of impact,
368 using the Gauss equations to fit ellipses to the distribution of the Pallas family in the a_m vs e_m and
369 a_m vs $\sin I_m$ spaces of the mean orbital elements.

370 Thermal parameters of our model included the bulk density $\rho = 2890 \text{ kg m}^{-3}$, the density
371 of surface layers (regolith) $\rho_{\text{surf}} = 1500 \text{ kg m}^{-3}$, the heat capacity $C = 680 \text{ J kg}^{-1} \text{ K}^{-1}$, the thermal
372 conductivity $K = 10^{-3} \text{ W m}^{-1} \text{ K}^{-1}$, the Bond albedo $A = 0.10$, and the infrared emissivity $\epsilon = 0.9$.
373 When unknown, diameters D were computed from absolute magnitudes H assuming the median
374 value of geometric albedo of the Pallas family members $p_V = 0.122^{61}$.

375 In order to compare our N-body integration with the observed family, we used the method
376 of Broz & Morbidelli (2019)⁶², which consists in rescaling the synthetic population to match the
377 observed SFD, and then computing the χ^2 for the number of objects counted in boxes defined in
378 the (a_m, e_m) space (Supplementary Fig. 7). The evolution of the $\chi^2(t)$ throughout our integration is
379 shown in Supplementary Fig. 8. It decreases from the initial value $\chi^2/N_{\text{box}} \simeq 3.6$ down to 1.35,
380 with the best-fit value corresponding to $t = 1.68 \text{ Ga}$. The uncertainty on the age was computed
381 from the scatter of the $\chi^2(t)$ values due to the random selection procedure, assuming the best-fit
382 value is acceptable. By doing so, we derived an estimate of the family's age of $t = 1.3$ to 1.9 Ga .

383 As a by-product, we computed the exponential decay time scales for bodies of various sizes,
384 which are necessary inputs for Monte-Carlo collisional models (see below). The values are $\tau =$
385 374, 419, 782, 1390, 2050, and 2130 Ma for the size bins between $D = 0.5, 1, 2, 5, 10, 20, 30 \text{ km}$,

386 respectively.

387 **The family-forming impact.** We then performed combined SPH/N-body simulations^{63–65}
388 aiming at deriving the impact parameters providing the best fit to the orbital distribution and SFD
389 of the Pallas family members, and allowing a direct comparison of the resulting impact features
390 with observations. Here again, we assumed that the Pallas family originated from a single large
391 collision. While multiple small events may eject enough material to produce the present-day fam-
392 ily, a large impact is needed to account for the size of the largest observed fragment ($D_{\text{lf}} \sim 20$ km).
393 In addition, fragments produced in a cratering event are usually smaller than the projectile, and
394 km-size fragments are continuously removed from the family by Yarkovsky drift^{57,58} and chaotic
395 diffusion over timescales of a few hundred million years, implying they cannot accumulate over
396 4 Ga. Consequently, our simulations, which are constrained by $D > 10$ km fragments, are not af-
397 fected by small cratering events.

398 Our model included a fragmentation without gravity⁶⁶ and gravitational reaccumulation⁶⁷.
399 We used Tillotson (1962)’s equation of state⁶⁸, vonMises (1913)’s yielding criterion⁶⁹, and Grady
400 & Kipp (1980)’s fracture model⁷⁰. Initial conditions included two spherical bodies (the target
401 and the projectile), with target size $D_{\text{pb}} = 513$ km, and impact velocity $v_{\text{imp}} = 12$ km s⁻¹. Our
402 simulations covered a range of specific energy ratios Q/Q_{D}^* , where Q_{D}^* denotes the strength from
403 the scaling law, provided in Supplementary Table 6. We used an SPH discretisation in space, with
404 number of particles $N_{\text{part}} \doteq 1.4 \times 10^5$, and a predictor–corrector discretisation in time. The time
405 step was limited by the Courant criterion, and to limit changes in energy, pressure and fracture

406 damage per time step to accurately control the integrations as described in Benz & Asphaug (1994,
407 1995)^{66,71}. Given the target size and v_{imp} , the chosen time span was 200 s. We used standard
408 artificial viscosity parameters $\alpha_{\text{av}} = 1.5$, $\beta_{\text{av}} = 3.0$, and a modification of the scalar damage \mathcal{D} ,
409 as in Ševeček et al. (2017)⁶⁵. Concerning the N-body part of the simulation, we used a handoff
410 relation $R_i = [3m_i/(4\pi\rho_i)]^{1/3}$, a tree-code with the opening angle $\theta = 0.5$ rad, and a hexadecapole
411 approximation for the gravity. We assumed a perfect merging. The time step was $\Delta t = 10^{-6}$ (in
412 $G = 1$ units), and the time span $50\,000 \Delta t$.

413 Our simulations covered a relevant range of outcomes, shown in Supplementary Fig. 9, from
414 weakly catastrophic to large cratering events. In every simulations the target was fully damaged.
415 The velocity field at the end of the fragmentation phase indicates that the first three higher-energy
416 impacts $Q/Q_{\text{D}}^* \geq 0.067$ affected essentially the whole surface of the target, while the last three
417 produced a large crater and only partial modification of the surface.

418 We determined the excavated mass before fall-back as the sum of all particles located above
419 $r > R + 30$ km, allowing for some expansion of the target. The simulations that better match
420 the observed SFD of the family (rows 3 and 4 in Supplementary Table 6) have excavated mass
421 $M_{\text{ex}} = 0.016$ to 0.027 (in M_{pb} units), implying the equatorial excavation is more likely to be
422 linked to the present-day Pallas family than the South-pole basin. From Supplementary Fig. 9, we
423 measured a transient crater size of at least 250 km, which can subsequently increase, possibly up
424 to the target size, during relaxation of the surface. However, the crater may not be well-preserved
425 in the highest-energy impacts due to substantial reaccumulation.

426 Supplementary Fig. 10 shows the SFD of the fragments after reaccumulation, assuming their
 427 final density is the same as before the impact ($\rho_0 = 2.89 \text{ g cm}^{-3}$). If we assume that the ejected frag-
 428 ments have retained their expanded densities, $\rho < \rho_0$, this would shift their SFD toward slightly
 429 larger D , possibly by a factor of 1.5. Consequently, lower-energy oblique impacts would pro-
 430 duce a better fit to the observed SFD. Our simulations covered a reasonable range of Q/Q_D^* , so
 431 that the largest fragments have sizes $D_{\text{lf}} = 14$ to 36 km that are relatively close to the observed
 432 value ($D_{\text{lf}} = 22.46$ km). The synthetic SFDs have significantly steeper slope than the observed
 433 one (approximately -5.0 vs -2.2), which indicates significant subsequent collisional and orbital
 434 evolution.

435 Next, the ejected mass was estimated as the sum of all fragments from the target. We did not
 436 include the projectile, which either vaporized, or whose remaining fragment escape the space of
 437 proper elements of the family. Ejected masses are comprised between 0.015 to 0.028 (M_{pb} units;
 438 Supplementary Table 6), which is comparable to M_{ex} .

439 **Evolution of the Size-Frequency Distribution of the family.** Independent constraints on
 440 the age of the family were derived using a Monte-Carlo collisional model, using as input the
 441 synthetic SFDs derived from our SPH simulations for the initial family. This method simulta-
 442 neously allows to estimate the probability that such a family is created over the course of evo-
 443 lution. We assumed constant intrinsic collisional probabilities $P_i = 2.86 \times 10^{-18}$, 2.17×10^{-18} ,
 444 and $2.87 \times 10^{-18} \text{ km}^{-2} \text{ a}^{-1}$ for the three relevant combinations of collisions (MB–MB, MB–Pallas,
 445 Pallas–Pallas), and mutual impact velocities $v_{\text{imp}} = 5.77$, 11.49 , and 13.05 km s^{-1} , computed ac-

446 cording to Bottke & Greenberg (1993)⁷². Our model includes a size-dependent dynamical decay
447 from Bottke et al. (2005)⁷³ for the main belt, and from our previous N-body simulation for the
448 Pallas family.

449 A number of additional parameters were specified, including the scaling law $Q_D^*(r)$, which
450 was taken from Benz & Asphaug (1999)⁷⁴ for basalt material, with $\rho = 2.89 \text{ g cm}^{-3}$, at the impact
451 velocity 5 km s^{-1} . This is inconsistent with typical velocities on Pallas, but it cannot be easily
452 improved unless a big matrix of simulations is computed. We also used a modification of the
453 parametric relation for the mass of the largest fragment $M_{lf}(Q/Q_D^*)$, which seems necessary for
454 small cratering events⁷⁵. Initial conditions are quite close to the observed SFD, except for the
455 synthetic family which is steeper (-5.0 cumulative). A discretisation in mass is performed with
456 a logarithmic factor 1.5. The output time step of the simulation was set to $\Delta t = 10 \text{ Ma}$, and the
457 nominal time spanned 4 Ga. At least 10 Monte-Carlo simulations were performed, because of
458 fractional probabilities of large breakups and lower-probability events.

459 Results are summarised in Supplementary Fig. 11. A typical time scale of a significant (10 %)
460 evolution of the family's SFD is of the order of 100 Ma, mostly due to dynamical decay and sec-
461 ondary MB–Pallas collisions. After 2 Ga of evolution, about a third of simulations produced syn-
462 thetic families with $D > 22.46 \text{ km}$ for the largest fragment. We therefore consider the Pallas family
463 to be a likely outcome of the equatorial excavation forming event. The event responsible for the
464 South-pole basin, on the other hand, requires up to 3-to-4 Ga of evolution owing to the steeper
465 SFD of the collisional fragments. This longer time is in contradiction with the simulated orbital

466 evolution of the family, implying that the South-pole basin is unlikely to relate to the present-day
467 Pallas family.

468 **Present-day composition of Pallas.** Combined with available mass estimates from the lit-
469 erature (Supplementary Table 4 and Supplementary Fig. 4), our 3D-shape model of Pallas returns
470 a bulk density of $2.89 \pm 0.08 \text{ g/cm}^3$, in perfect agreement with the grain density of CM chondrite
471 meteorites ($2.90 \pm 0.08 \text{ g/cm}^3$)²¹ assuming near zero porosity in the interior of Pallas. Whereas CM
472 chondrites exhibit the same hydration signature in the 3- μm wavelength range as Pallas⁶, these
473 meteorites are usually linked to Ch/Cgh-type asteroids^{22,76,77} and have distinct spectral properties
474 from Pallas in the visible and near-infrared (0.4-2.5 μm). Specifically, Pallas is bluer and brighter
475 than most CM chondrites and it does not exhibit the 0.7-0.9- μm absorption features that is present
476 in the meteorite spectra.

477 A direct link between Pallas and CM chondrites therefore does not appear obvious. It is
478 possible, however, that Pallas and the parent bodies of CM chondrites accreted from the same
479 initial material, as suggested by their similar densities, and that their spectral differences come
480 from distinct subsequent thermal and collisional evolution owing to Pallas' large size and distinct
481 collisional environment. In particular, frequent high-energy impacts and micro-meteorite bom-
482 bardement on Pallas could have led to partial dehydration of its surface, which could explain its
483 bluer and brighter spectrum and the lack of phyllosilicate signatures in the visible. On the other
484 hand, the 3- μm signature would have been preserved because of its much deeper and broader pro-
485 file. Along these lines, laboratory experiments have shown that artificially heated CM chondrites

486 usually exhibit bluer, brighter (although not as bright as Pallas) and more featureless spectra^{78,79}.
487 Based on these considerations, it appears possible that Pallas represents the parent body of heated
488 CM chondrites, for which no parent body has been identified so far.

489 Pallas' derived bulk density is further higher than Ceres' ($2.16 \pm 0.01 \text{ g/cm}^3$)², suggesting a
490 lower water-to-rock ratio, in agreement with its higher and seemingly more stable topography. A
491 lower water content for Pallas with respect to Ceres is also in agreement with the survival of the
492 Pallas family members over several hundred million years, while the lack of a Ceres family points
493 towards rapid sublimation of impact fragments from Ceres⁸⁰.

494 **Initial rock-to-ice ratio of Pallas.** Assuming Pallas accreted from a mixture of anhydrous
495 dust and ice, two distinct evolutionary pathways must be considered when assessing its early in-
496 ternal evolution. In the first scenario, Pallas accreted with about the same bulk water content as
497 inferred from its measured density. This leads to a low water-to-rock ratio ($W:R < 1$) in the transient
498 ocean generated by the decay of short-lived radioisotopes. In that case, Pallas did not differentiate,
499 and its current surface would represent a collisionally evolved version of its original one. In the
500 alternate case where Pallas' initial $W:R$ was high ($\gg 1$), thermophysical modelling predicts the for-
501 mation of an icy outer shell through the separation of water from the silicates, upward flowing and
502 freezing towards the surface. This icy shell being missing at present implies it would have been
503 progressively removed by collisions exposing fresh ice and thus triggering their sublimation. In
504 that scenario, today's Pallas surface would represent the hydrated mantle of the proto-Pallas.

505 Considering that the measured density of Pallas is fully compatible with CM chondrites, as

506 well as with its predicted mineralogy in the low W:R scenario studied by Castillo-Rogez et al.
 507 (2018)⁸¹, which is also consistent with aqueous alteration conditions inferred for CM chondrites⁸²,
 508 we favour the low W:R scenario for its formation and evolution. Importantly, the modelled min-
 509 eralogy includes small fractions of salts (e.g., carbonates, chlorides), the presence of which could
 510 explain both the higher albedo of the Pallas family compared to other B-type asteroids^{61,83}, and
 511 albedo variations seen on the surface of Pallas.

512 **Formation time and interior of Pallas.** Whether Pallas' internal temperature reached the
 513 silicate dehydration threshold (~820 K) depends on its time of formation. One-dimensional ther-
 514 mal conduction was modelled using the approach developed by Castillo-Rogez et al. (2007)⁸⁴ and
 515 applied to a variety of bodies, including Pallas⁸⁵. Specifically, heat was transferred by conduction
 516 with the following equation:

$$\frac{\partial (k(T) \partial(T)/r)}{\partial r} + \frac{2}{r} \left(k(T) \frac{\partial T(r)}{\partial r} \right) = \rho(r) C_p(T) \frac{dT(r)}{dt} - H(r) \quad (1)$$

517 where T is temperature (in Kelvin), r local radius, k thermal conductivity, ρ material density,
 518 C_p specific heat, t time, H internal heating (i.e., radioisotope decay heat). Calculation of the
 519 radioisotope decay heat, the main heat source for Pallas, can be found in Supplementary Table 7.
 520 The properties of the materials used in the modelling are listed in Supplementary Table 8. Pure
 521 serpentine has a thermal conductivity of about 2.5 W/m/K while anhydrous silicates (olivine and
 522 pyroxene) have thermal conductivities up to 5 W/m/K⁸⁶. The latter could be present if aqueous

523 alteration was partial. Also, the presence of iron-rich compounds in the rock (like iron sulfide
524 and oxides) could increase the thermal conductivity further. In this study, we covered a range of
525 thermal conductivities for the mantle from 0.5 to 2.5 W/m/K under the assumption that aqueous
526 alteration might be advanced.

527 Using this model, we found that partial dehydration of the core of Pallas occurs for times
528 of formation $T_0 < 2.5$ Ma after the formation of CAIs (Supplementary Fig. 5). Provided that the
529 proposed association between CM chondrite meteorites and Pallas is correct, and considering the
530 isotopic ages of CM chondrites (mostly > 3.0 Ma after the formation of CAIs)²³, we conclude that
531 the amount of radioisotopes accreted by Pallas was too low to trigger large-scale silicate dehydra-
532 tion and the differentiation of a denser silicate core below a hydrated mantle, thus implying a rather
533 homogeneous interior. This finding is consistent with previous studies that found the primordial
534 internal structure of CM parent bodies to be globally homogeneous^{22, 87–89}. However, considering
535 Pallas' large size, early partial differentiation (water separation and upward flow) must have oc-
536 curred in its interior and could explain the high albedo and its variations by an enrichment in salts
537 through aqueous alteration.

538 The presence of salts in Pallas would further provide a natural explanation to the diversity
539 of sodium contents measured in the Geminids meteor stream^{28–32}. The Geminids are believed to
540 originate from the 5–6-km Apollo-type asteroid (3200) Phaethon³³, a proposed fragment from
541 the Pallas family that would have been emplaced in the near-Earth space following gravitational
542 interactions with the Jovian mean-motion resonances^{26, 27}. The proposed link between Pallas and

543 Phaethon, however, remains matter of debate: while the spectra of Phaethon, Pallas, and the Pallas
544 family members are strikingly similar in the visible and near-infrared, estimates of the albedo of
545 Phaethon based on thermal measurements show some controversy: some values are consistent
546 with those derived for Pallas and the Pallas family members⁹⁰⁻⁹², while others are significantly
547 lower⁹³. Polarimetric studies provide an independent insight into this controversy as the albedo of
548 an asteroid can be evaluated from its maximum value of linear polarization degree P_{\max} ⁹⁴ and/or
549 from its polarimetric slope h ^{95,96}. High P_{\max} values usually correspond to low albedos that are
550 typical of C-type asteroids^{94,97}. In case of Phaethon, however, the high value of P_{\max} might be
551 better explained by a large average regolith grain size and perhaps also a large surface porosity⁹⁴.
552 Albedo estimates derived from the polarimetric slope h , on the other hand, are less dependent
553 on particle size. In the case of Phaethon, the albedo derived from the h value is intermediate
554 ($14\pm 4\%$)⁹⁸, in agreement with Pallas.

555 Finally, it should be noted that Phaethon does not exhibit the $3\text{-}\mu\text{m}$ absorption band that
556 characterises Pallas⁹⁹. Whether this difference is due to the thermal evolution of Phaethon's surface
557 (e.g., the complete dehydration of surface minerals) in the near-Earth space, or to the fact that
558 Phaethon is not genetically linked to Pallas, remains an open question that should be addressed
559 by the future DESTINY+ fly-by mission to Phaethon¹⁰⁰ or by acquiring high-quality mid-infrared
560 spectra of both Pallas and Phaethon with the James-Webb Space telescope.

561 **Data availability.** As soon as papers for our large program are accepted for publication, we make
562 the corresponding reduced and deconvolved AO images and 3D shape models publicly available

563 at <http://observations.lam.fr/astero/>.

564 **Code availability.** The code used to generate the 3D shape is available at [https://github.com/](https://github.com/matvii/ADAM)
565 [matvii/ADAM](https://github.com/matvii/ADAM). The modified SWIFT integrator used to model the orbital evolution of the Pallas
566 family is available at <http://sirrah.troja.mff.cuni.cz/~mira/mp/>.

568 34. Liu, Z. *et al.* A global database and statistical analyses of (4) Vesta craters. *Icarus* **311**,
569 242–257 (2018).

570 35. Marchi, S. *et al.* The Violent Collisional History of Asteroid 4 Vesta. *Science* **336**, 690 (2012).

571 36. Marchi, S. *et al.* The missing large impact craters on Ceres. *Nat. Commun.* **7**, 12257 (2016).

572 37. Pasckert, J. H. *et al.* Geologic mapping of the Ac-2 Coniraya quadrangle of Ceres from
573 NASA's Dawn mission: Implications for a heterogeneously composed crust. *Icarus* **316**, 28–
574 45 (2018).

575 38. Morbidelli, A., Bottke, W. F., Nesvorný, D. & Levison, H. F. Asteroids were born big. *Icarus*
576 **204**, 558–573 (2009). 0907.2512.

577 39. Cibulková, H., Brož, M. & Benavidez, P. G. A six-part collisional model of the main asteroid
578 belt. *Icarus* **241**, 358–372 (2014). 1407.6143.

579 40. Werner, S. C. & Ivanov, B. A. Exogenic Dynamics, Cratering and Surface Ages. In *Treatise*
580 *on Geophysics, 2nd Edition*, 327–365 (Elsevier, 2015).

- 581 41. Viikinkoski, M. *et al.* VLT/SPHERE- and ALMA-based shape reconstruction of asteroid (3)
582 Juno. *Astron. Astrophys.* **581**, L3 (2015).
- 583 42. Viikinkoski, M. *Shape Reconstruction from Generalized Projections*. Ph.D. thesis, Tampere
584 University of Technology (2016).
- 585 43. Marsset, M. *et al.* 3D shape of asteroid (6) Hebe from VLT/SPHERE imaging: Implications
586 for the origin of ordinary H chondrites. *Astron. Astrophys.* **604**, A64 (2017).
- 587 44. Hanuš, J., Marchis, F., Viikinkoski, M., Yang, B. & Kaasalainen, M. Shape model of aster-
588 oid (130) Elektra from optical photometry and disk-resolved images from VLT/SPHERE and
589 Nirc2/Keck. *Astron. Astrophys.* **599**, A36 (2017).
- 590 45. McLean, I. S. & Chaffee, F. H. Instrum. for the Keck Observatory. In Iye, M. & Moorwood,
591 A. F. (eds.) *Optical and IR Telescope Instrum. and Detectors*, vol. 4008 of *Proc. SPIE*, 2–7
592 (2000).
- 593 46. Burns, J. A. & Safronov, V. S. Asteroid nutation angles. *Mon. Not. R. Astron. Soc.* **165**, 403
594 (1973).
- 595 47. Chambat, F., Ricard, Y. & Valette, B. Flattening of the Earth: further from hydrostaticity than
596 previously estimated. *Geophys. J. Int.* **183**, 727–732 (2010).
- 597 48. Rambaux, N., Chambat, F. & Castillo-Rogez, J. C. Third-order development of shape, gravity,
598 and moment of inertia for highly flattened celestial bodies. Application to Ceres. *Astron.*
599 *Astrophys.* **584**, A127 (2015).

- 600 49. Lanzano, P. The Equilibrium of a Rotating Body of Arbitrary Density. *Astrophys. Space Sci.*
601 **29**, 161–178 (1974).
- 602 50. Nesvorný, D., Brož, M. & Carruba, V. Identification and Dynamical Properties of Asteroid
603 Families. In *Asteroids IV*, 297–321 (University of Arizona Press, Tucson, 2015).
- 604 51. Mainzer, A. K. *et al.* NEOWISE Diameters and Albedos V1.0. *NASA Planet. Data Syst.* **247**,
605 EAR–A–COMPIL–5–NEOWISEDIAM–V1.0 (2016).
- 606 52. Ivezić, Ž. *et al.* Color Confirmation of Asteroid Families. *Astron. J.* **124**, 2943–2948 (2002).
607 [astro-ph/0208098](https://arxiv.org/abs/astro-ph/0208098).
- 608 53. Quinn, T. R., Tremaine, S. & Duncan, M. A three million year integration of the earth’s orbit.
609 *Astron. J.* **101**, 2287–2305 (1991).
- 610 54. Levison, H. F. & Duncan, M. J. The long-term dynamical behavior of short-period comets.
611 *Icarus* **108**, 18–36 (1994).
- 612 55. Brož, M., Vokrouhlický, D., Morbidelli, A., Nesvorný, D. & Bottke, W. F. Did the Hilda
613 collisional family form during the late heavy bombardment? *Mon. Not. R. Astron. Soc.* **414**,
614 2716–2727 (2011). [1109.1114](https://arxiv.org/abs/1109.1114).
- 615 56. Vokrouhlický, D. Diurnal Yarkovsky effect as a source of mobility of meter-sized asteroidal
616 fragments. I. Linear theory. *Astron. Astrophys.* **335**, 1093–1100 (1998).
- 617 57. Vokrouhlický, D. & Farinella, P. The Yarkovsky Seasonal Effect on Asteroidal Fragments: A
618 Nonlinearized Theory for Spherical Bodies. *Astron. J.* **118**, 3049–3060 (1999).

- 619 58. Čapek, D. & Vokrouhlický, D. The YORP effect with finite thermal conductivity. *Icarus* **172**,
620 526–536 (2004).
- 621 59. Farinella, P., Froeschlé, C. & Gonczi, R. Meteorite Delivery and Transport. In Milani, A.,
622 di Martino, M. & Cellino, A. (eds.) *Asteroids, Comets, Meteors 1993*, vol. 160 of *IAU Symp.*,
623 205 (1994).
- 624 60. Alí-Lagoa, V. *et al.* Differences between the Pallas collisional family and similarly sized B-
625 type asteroids. *Astron. Astrophys.* **591**, A14 (2016).
- 626 61. Brož, M. & Morbidelli, A. A study of 3-dimensional shapes of asteroid families with an
627 application to Eos. *Icarus* **317**, 434–441 (2019). 1810.04113.
- 628 62. Benz, W. & Asphaug, E. Impact simulations with fracture. I - Method and tests. *Icarus* **107**,
629 98 (1994).
- 630 63. Jutzi, M., Holsapple, K., Wünneman, K. & Michel, P. Modeling asteroid collisions and impact
631 processes. In *Asteroids IV*, 679–699 (University of Arizona Press, Tucson, 2015).
- 632 64. Ševeček, P. *et al.* SPH/N-Body simulations of small ($D = 10\text{km}$) asteroidal breakups and im-
633 proved parametric relations for Monte-Carlo collisional models. *Icarus* **296**, 239–256 (2017).
- 634 65. Benz, W. & Asphaug, E. Impact simulations with fracture. I - Method and tests. *Icarus* **107**,
635 98 (1994).
- 636 66. Richardson, D. C., Quinn, T., Stadel, J. & Lake, G. Direct Large-Scale N-Body Simulations
637 of Planetesimal Dynamics. *Icarus* **143**, 45–59 (2000).

- 638 67. Tillotson, J. H. Metallic equations of state for hypervelocity impact. *Gen. Atomic Rep. GA-*
639 *3216* (1962).
- 640 68. von Mises, R. Mechanik der festen krper im plastisch- deformablen zustand. *Nachrichten von*
641 *der Ges. der Wissenschaften zu Göttingen, Math.-Phys. Klasse* 582–592 (1913).
- 642 69. Grady, D. & Kipp, M. Continuum modelling of explosive fracture in oil shale. *Int. J. Rock.*
643 *Mech. Min.* **17**, 147–157 (1980).
- 644 70. Benz, W. & Asphaug, E. Simulations of brittle solids using smooth particle hydrodynamics.
645 *Comput. Phys. Commun.* **87**, 253–265 (1995).
- 646 71. Bottke, W. F. & Greenberg, R. Asteroidal collision probabilities. *Geophys. Res. Lett.* **20**,
647 879–881 (1993).
- 648 72. Bottke, W. F. *et al.* Linking the collisional history of the main asteroid belt to its dynamical
649 excitation and depletion. *Icarus* **179**, 63–94 (2005).
- 650 73. Benz, W. & Asphaug, E. Catastrophic Disruptions Revisited. *Icarus* **142**, 5–20 (1999). [arXiv:](https://arxiv.org/abs/astro-ph/9907117)
651 [astro-ph/9907117](https://arxiv.org/abs/astro-ph/9907117).
- 652 74. Vernazza, P. *et al.* The impact crater at the origin of the Julia family detected with
653 VLT/SPHERE? *Astron. Astrophys.* **618**, A154 (2018).
- 654 75. Vilas, F. & Gaffey, M. J. Phyllosilicate absorption features in main-belt and outer-belt asteroid
655 reflectance spectra. *Science* **246**, 790–792 (1989).

- 656 76. Fornasier, S., Lantz, C., Barucci, M. A. & Lazzarin, M. Aqueous alteration on main belt
657 primitive asteroids: Results from visible spectroscopy. *Icarus* **233**, 163–178 (2014).
- 658 77. Spectral reflectance properties of carbonaceous chondrites 4: Aqueously altered and thermally
659 metamorphosed meteorites. *Icarus* **220**, 586–617 (2012).
- 660 78. Lantz, C. *et al.* Ion irradiation of carbonaceous chondrites: A new view of space weathering
661 on primitive asteroids. *Icarus* **285**, 43–57 (2017).
- 662 79. Rivkin, A. S., Asphaug, E. & Bottke, W. F. The Case of the Missing Ceres Family. *Icarus*
663 1–54 (2014).
- 664 80. Castillo-Rogez, J. *et al.* Insights into Ceres’s evolution from surface composition. *Meteorit.*
665 *Planet. Sci* **53**, 1820–1843 (2018).
- 666 81. Howard, K. T., Benedix, G. K., Bland, P. A. & Cressey, G. Modal mineralogy of CM chon-
667 drites by X-ray diffraction (PSD-XRD): Part 2. Degree, nature and settings of aqueous alter-
668 ation. *Geochim. Cosmochim. A.* **75**, 2735–2751 (2011).
- 669 82. Alí-Lagoa, V. *et al.* Physical properties of B-type asteroids from WISE data. *Astron. Astrophys.*
670 **554**, A71 (2013). 1303.5487.
- 671 83. Castillo-Rogez, J. C. *et al.* Iapetus’ geophysics: Rotation rate, shape, and equatorial ridge.
672 *Icarus* **190**, 179–202 (2007).
- 673 84. Schmidt, B. E. & Castillo-Rogez, J. C. Water, heat, bombardment: The evolution and current
674 state of (2) Pallas. *Icarus* **218**, 478–488 (2012).

- 675 85. Opeil, C. P., Consolmagno, G. J. & Britt, D. T. The thermal conductivity of meteorites: New
676 measurements and analysis. *Icarus* **208**, 449–454 (2010).
- 677 86. Dufresne, E. R. & Anders, E. On the chemical evolution of the carbonaceous chondrites.
678 *Geochim. Cosmochim. A.* **26**, 1085–1114 (1962).
- 679 87. Bland, P. A. & Travis, B. J. Giant convecting mud balls of the early solar system. *Sci. Advances*
680 **3**, e1602514 (2017).
- 681 88. Carry, B. *et al.* Homogeneous internal structure of CM-like asteroid (41) Daphne. *Astron.*
682 *Astrophys.* **623**, A132 (2019). 1901.01890.
- 683 89. Alí-Lagoa, V. *et al.* Differences between the Pallas collisional family and similarly sized B-
684 type asteroids. *Astron. Astrophys.* **591**, A14 (2016).
- 685 90. Hanuš, J. *et al.* Shape, size, physical properties and nature of low-perihelion near-Earth aster-
686 oid (3200) Phaethon. In *AAS/Division for Planet. Sci. Meeting Abstr.*, vol. 48 of *AAS/Division*
687 *for Planet. Sci. Meeting Abstr.*, 516.08 (2016).
- 688 91. Masiero, J. R., Wright, E. L. & Mainzer, A. K. Thermophysical Modeling of NEOWISE
689 Observations of DESTINY⁺ Targets Phaethon and 2005 UD. *Astron. J.* **158**, 97 (2019). 1907.
690 04518.
- 691 92. Karetá, T. *et al.* Rotationally Resolved Spectroscopic Characterization of Near-Earth Object
692 (3200) Phaethon. *Astron. J.* **156**, 287 (2018). 1810.11157.

- 693 93. Ito, T. *et al.* Extremely strong polarization of an active asteroid (3200) phaethon. *Nat. Com-*
694 *mun.* **9**, 2486 (2018). URL <https://doi.org/10.1038/s41467-018-04727-2>.
- 695 94. Cellino, A. *et al.* On the calibration of the relation between geometric albedo and polarimetric
696 properties for the asteroids. *Mon. Not. R. Astron. Soc.* **451**, 3473–3488 (2015). 1506.00554.
- 697 95. Lupishko, D. F. Generalized Calibration of the Polarimetric Albedo Scale of Asteroids. *Solar*
698 *Syst. Res.* **52**, 98–114 (2018).
- 699 96. Devogèle, M. *et al.* The phase-polarization curve of asteroid (3200) Phaethon. *Mon. Not. R.*
700 *Astron. Soc.* (2018). 1806.05277.
- 701 97. Shinnaka, Y. *et al.* Inversion Angle of Phase-polarization Curve of Near-Earth Asteroid (3200)
702 Phaethon. *Astrophys. J. Lett.* **864**, L33 (2018). 1808.05746.
- 703 98. Takir, D. *et al.* 3-um Spectroscopy of Asteroid (3200) Phaethon: Implications for B-Asteroids.
704 In *Lunar and Planet. Sci. Conf.*, vol. 49 of *Lunar and Planet. Sci. Conf.*, 2624 (2018).
- 705 99. Arai, T. *et al.* DESTINY+ Mission: Flyby of Geminids Parent Asteroid (3200) Phaethon and
706 In-Situ Analyses of Dust Accreting on the Earth. In *Lunar and Planet. Sci. Conf.*, vol. 49 of
707 *Lunar and Planet. Sci. Conf.*, 2570 (2018).